Numerical Simulation of Phase Space Advection in Gyrokinetic Models of Fusion Plasmas

M. R. Dorr[1], R. H. Cohen[2], P. Colella[3], M. A. Dorf[2], J. A. F. Hittinger[1], and D. F. Martin[3]

[1]Center for Applied Scientific Computing, Lawrence Livermore National Laboratory, 7000 East Avenue L-561, Livermore, CA 94550[*]

[2]Fusion Energy Program, Lawrence Livermore National Laboratory, 7000 East Avenue L-630, Livermore, CA 94550. [3]Applied Numerical Algorithms Group, Lawrence Berkeley National Laboratory, One Cyclotron Road Mail Stop 50A-1148, Berkeley, CA 94720[†]

Abstract. We describe our progress in the development of a fourth-order, finite-volume discretization of a nonlinear, full-f gyrokinetic Vlasov-Poisson system in mapped coordinates. The approach treats the configuration and velocity components of phase space on an equal footing, using a semi-discretization with limited centered fluxes combined with a fourth-order Runge Kutta integration. The algorithm has been implemented in a new code named COGENT, which is built on the Chombo Adaptive Mesh Refinement library being developed by the SciDAC APDEC project. The algorithm and code have been tested on geodesic acoustic mode problems in a standard equilibrium magnetic geometry by comparing damping rates and frequencies with those predicted by theoretical dispersion analyses. Convergence tests are also performed to verify the expected increase in accuracy as the phase space grid was refined.

1. Introduction

The ability to computationally model the behavior of the edge plasma in fusion reactors is a key component in the development of a whole device predictive simulation capability.

Among the features that distinguish the edge from the core is the development of a region of steep gradients in the density and temperature profiles called the pedestal, the height of which determines the quality of plasma confinement, and hence fusion gain. A kinetic plasma model in needed in this region (Figure 1), because the radial width of the pedestal observed in experiments is comparable to the radial width of individual particle orbits (leading to large distortions of the local distribution functions from a Maxwellian), while the mean free path can be comparable to the scale length for temperature variations along the magnetic field (violating the assumptions underlying a collisional fluid model).

Because of the large number of independent variables in a fully kinetic model, as well as the fast time scale represented by the ion gyrofrequency, gyrokinetic models (which average over fast gyro motion about field lines) have been developed to facilitate numerical treatments. Continuum models consist of a Boltzmann equation for evolving plasma species distribution functions in a particular coordinate system

[*] This work performed under the auspices of the U.S. Department of Energy by Lawrence Livermore National Laboratory under Contract DE-AC52-07NA27344

[†] Research supported by the Office of Advanced Scientific Computing Research of the US Department of Energy under contract number DE-AC02-05CH11231.

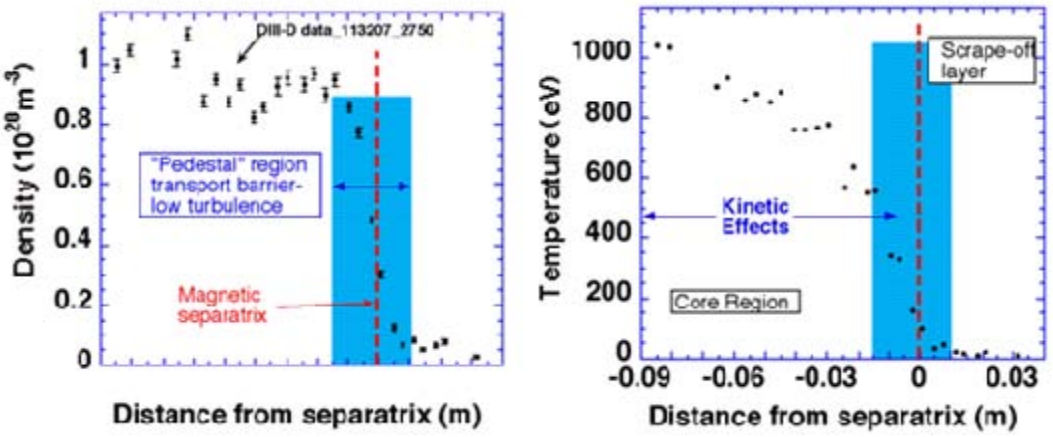

Figure 1. DIII-D pedestal [13].

combined with some variant of Maxwell's equations. Gyrokinetic codes such as GENE[9, 10], GS2[6,11] and GYRO[1, 3, 2] have been successfully employed to model core plasmas for many years. In addition to requiring simpler geometries, these codes exploit the fact that in the core, distribution functions are typically small perturbations δf about a known Maxwellian distribution f_0, providing a simpler, and even sometimes linear, model. To model the edge plasma all the way to the reactor walls, a method to solve nonlinear gyrokinetic models for the entire distribution function (so-called full-*f*) in edge-relevant geometries is needed.

In this paper, we summarize our progress to date in the development and application of new algorithmic methodologies in the solution of a nonlinear, full-*f*, gyrokinetic Vlasov-Poisson system. Beginning with a conservative formulation, the system is treated as a nonlinear advection equation in a 4D (2 configuration space + 2 velocity space coordinates) or 5D (3 configuration space + 2 velocity space coordinates) phase space. A semi-discretization is employed based on a recently developed formalism [4] for the creation of arbitrarily high-order finite-volume spatial discretizations in mapped coordinates. In the present context, mapped coordinates enable the use of a multiblock, locally rectangular computational domain, one of whose coordinates is aligned with magnetic flux surfaces. The use of a finite volume formulation naturally enables the discrete enforcement of conservation, whereas a fourth-order discretization provides for more efficient gridding of phase space and reduced numerical dissipation for long-time integration. We demonstrate the performance of the algorithms on the simulation of geodesic acoustic modes, which are eigenmodes of the gyrokinetic Vlasov-Poisson system.

2. The gyrokinetic Vlasov-Poisson system

We adopt the full *f* gyrokinetic model of [8]:

$$\frac{\partial (B_{\parallel\alpha}^* f_\alpha)}{\partial t} + \boldsymbol{\nabla}_{\mathbf{R}} \cdot \left(\dot{\mathbf{R}}_\alpha B_{\parallel\alpha}^* f_\alpha \right) + \frac{\partial}{\partial v_\parallel} \left(\dot{v}_{\parallel\alpha} B_{\parallel\alpha}^* f_\alpha \right) = 0, \tag{1}$$

where

$$\dot{\mathbf{R}}_\alpha \equiv \dot{\mathbf{R}}_\alpha(\mathbf{R}, v_\parallel, \mu, t) \equiv \frac{v_\parallel}{B_{\parallel\alpha}^*} \mathbf{B}_\alpha^* + \frac{\rho_L}{Z_\alpha B_{\parallel\alpha}^*} \mathbf{b} \times \mathbf{G}_\alpha, \tag{2}$$

$$\dot{v}_{\parallel\alpha} \equiv \dot{v}_{\parallel\alpha}(\mathbf{R}, v_\parallel, \mu, t) \equiv -\frac{1}{m_\alpha B_{\parallel\alpha}^*} \mathbf{B}_\alpha^* \cdot \mathbf{G}_\alpha, \tag{3}$$

and

$$\mathbf{B}_\alpha^* \equiv \mathbf{B}_\alpha^*(\mathbf{R}, v_\parallel) \equiv \mathbf{B} + \rho_L \frac{m_\alpha v_\parallel}{Z_\alpha} \nabla_{\mathbf{R}} \times \mathbf{b}, \tag{4}$$

$$B_{\parallel\alpha}^* \equiv B_{\parallel\alpha}^*(\mathbf{R}, v_\parallel) \equiv \mathbf{b} \cdot \mathbf{B}_\alpha^*, \tag{5}$$

$$\mathbf{G}_\alpha \equiv \mathbf{G}_\alpha(\mathbf{R}, \mu, t) \equiv Z_\alpha \nabla_{\mathbf{R}} \Phi + \frac{\mu}{2} \nabla_{\mathbf{R}} B. \tag{6}$$

The unknown quantity $f_\alpha \equiv f_\alpha(\mathbf{R}_\alpha, v_{||}, \mu, t)$ is the distribution function of the α^{th} plasma species in gyrocenter phase space coordinates ($\mathbf{R}_\alpha, v_{||}, \mu$), whose equations of motion are given by (2)-(6). To simplify the exposition here, we have neglected the drift due to the equilibrium potential. We have also assumed a particular normalization that nondimensionalizes all quantities. For example, the quantity ρ_L appearing in the last term of (2) denotes the ion Larmor radius of the normalizing reference species relative to the chosen normalizing length scale.

Gyrocenter coordinates play a key role in gyrokinetic models in two important ways. First, they reduce what would otherwise be a six-dimensional phase space to five dimensions: $\mathbf{R}_\alpha$ is the three-dimensional configuration space coordinate, $v_{||}$ is the velocity space component along field lines, and the magnetic moment $\mu \equiv m_\alpha v_\perp^2 / 2B$ is related to the velocity $v_\perp$ perpendicular to field lines. Through the use of asymptotic orderings, gyrocenter coordinates are specifically constructed so as to make the distribution function f symmetric with respect to gyrophase. The latter component, which would have been the third velocity component, can then be ignored. The magnetic moment μ, an adiabatic invariant, is assumed to be constant in the development of gyrokinetic theories, which is why no evolution equation appears for it. The second benefit of gyrocenter coordinates is that the gyrofrequency is eliminated, which would otherwise represent a fast time scale that would need to be resolved. Because gyrocenter coordinates are developed as a Hamiltonian dynamical system, they satisfy the area preserving property

$$\nabla_{\mathbf{R}} \cdot \left(B_{\parallel\alpha}^* \dot{\mathbf{R}}_\alpha \right) + \frac{\partial}{\partial v_\parallel} \left(B_{\parallel\alpha}^* \dot{v}_{\parallel\alpha} \right) = 0, \tag{7}$$

where $B_{||}^*{}_\alpha$ is the Jacobian of the mapping between lab frame and gyrocenter coordinates. As noted in [8], the gyrokinetic Vlasov equation can therefore be expressed in either convective or conservative form. We choose the latter with the objective of achieving a correspondingly conservative numerical discretization.

The potential Φ in (6) is evaluated by solving some form of Maxwell's equations. Here, we assume an electrostatic model obtained by the addition of Poisson's equation to the Vlasov system (1)-(6). The potential then depends only upon the charge density of the distribution functions f_α. A difficulty arises, however, from the fact that the f_α are only known in gyrocenter coordinates, whereas the Poisson equation is posed in the lab frame. The velocity integral used to compute the ion charge density must therefore be split into two pieces. In the long wavelength limit $k\rho \ll 1$, where k is the magnetic field wave number and ρ is the ion gyroradius, the gyrokinetic Poisson equation is

$$\nabla_{\mathbf{X}} \cdot \left\{ \left[\lambda_D^2 \mathbf{I} + \rho_L^2 \sum_\alpha \frac{Z_\alpha \bar{n}_\alpha}{m_\alpha \Omega_\alpha^2} \left(\mathbf{I} - \mathbf{b}\mathbf{b}^T \right) \right] \nabla_{\mathbf{X}} \Phi \right\} = n_e - \sum_\alpha Z_\alpha \bar{n}_\alpha, \tag{8}$$

where $\nabla_{\mathbf{X}}$ denotes the gradient with respect to the normalized lab frame coordinate and λ_D is the normalized Debye length. The quantity

$$\bar{n}_\alpha(x,t) \equiv \frac{1}{m_\alpha} \int f_\alpha(x, v_\parallel, \mu, t) B^*_\parallel(x, v_\parallel) dv_\parallel d\mu \tag{9}$$

is the ion gyrocenter density, which is the gyrophase independent part of the integration of the gyrocenter distribution function f_α over velocity. The second term in the left-hand side of (8) is the polarization density, which is the gyrophase-dependent part of the velocity integration of f_α . Since this piece depends upon the potential, we must combine it with the usual Laplacian (the first term in (8)) in the construction of the linear operator to be solved for Φ. Here, **b** denotes the unit vector in the direction of the magnetic field, Z_α is the charge state, m_α is the mass and Ω_α is the gyrofrequency. We note that for typical tokamak parameters, $\lambda_D \ll \rho_L$, and hence the polarization density term dominates. Because the electron gyroradius is small, a similar splitting of the electron density is omitted.

The gyrokinetic Vlasov-Poisson system is posed in a domain defined by the tokamak magnetic geometry, which is comprised of field lines lying on concentric flux surfaces. Since there are large variations of plasma parameters along and across field lines, there is strong motivation to discretize in coordinates where at least one of the coordinate directions is defined by the flux surfaces. As depicted in Figure 2, a natural choice is a mapped multiblock coordinate system, where the blocks correspond to the logically distinct core, scrapeoff layer and private flux regions. Within each block, a rectangular coordinate system can be employed, which facilitates efficient and accurate discretizations and domain decompositions over processors.

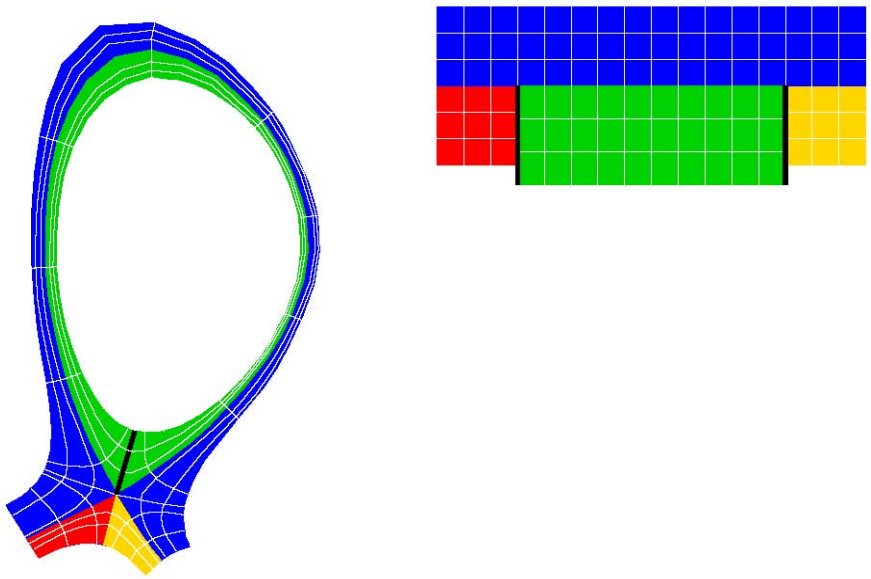

Figure 2. Single null geometry (left) and multi-block, locally rectangular computational domain (right).

We are therefore led to consider the discretization of the gyrokinetic Vlasov-Poisson system (1)-(6) in a mapped coordinate system. Among our requirements is a conservative formulation, thereby discretely expressing the phase space conservation law (1). A second requirement is high-order accuracy, enabling a more efficient deployment of degrees of freedom in discretizing the high-dimensional phase space. A high-order method is also important for reducing numerical dissipation in long-time integrations. Additional requirements include enforcement of positivity for the distribution functions f_α and an efficient solver for the gyrokinetic Poisson equation.

3. High-order, finite volume discretization in mapped coordinates

Next, we summarize a general approach for the systematic development of high-order finite volume discretizations in mapped coordinates. More complete details are contained in [4].

Suppose that we have a smooth mapping $\boldsymbol{X}$ from the unit cube onto the spatial domain Ω:

$$\boldsymbol{X} = \boldsymbol{X}(\boldsymbol{\xi}),\ \boldsymbol{X} : [0,1]^3 \rightarrow \Omega.$$

Given this mapping, the divergence of a vector field on Ω can be written in terms of derivatives in $[0, 1]^3$, which will serve as our computational domain. That is,

$$\boldsymbol{\nabla}_{\boldsymbol{x}} \cdot \boldsymbol{F} = \frac{1}{J} \boldsymbol{\nabla}_{\boldsymbol{\xi}} \cdot (\boldsymbol{N}^T \boldsymbol{F}), \tag{10}$$

$$J = det(\boldsymbol{\nabla}_{\boldsymbol{\xi}} \boldsymbol{X})\ ,\ \boldsymbol{N}^T_{p,q} = det((\boldsymbol{\nabla}_{\boldsymbol{\xi}} \boldsymbol{X})(p|\boldsymbol{e}^q)), \tag{11}$$

where $\boldsymbol{A}(p|v)$ denotes the matrix obtained by replacing the p^{th} row of the matrix $\boldsymbol{A}$ by the vector v and e^q is the unit vector in the q-th direction. The relationship (10) is an easy consequence of the chain rule, equality of mixed partials, and Cramer's rule.

In a finite volume approach, Ω is discretized as a union of control volumes. For Cartesian grid finite volume methods, a control volume Vi takes the form

$$V_{\boldsymbol{i}} = \left[\left(\boldsymbol{i} - \frac{1}{2}\boldsymbol{u} \right) h, \left(\boldsymbol{i} + \frac{1}{2}\boldsymbol{u} \right) h \right]\ ,\ \boldsymbol{i} \in \mathbb{Z}^3\ ,\ \boldsymbol{u} = (1,1,1),$$

where h is the grid spacing. When using mapped coordinates, we define control volumes in Ω as the images $X(V_i)$ of the cubic control volumes $V_i \subset [0, 1]^3$. Then, by changing variables and applying the divergence theorem, we obtain the flux divergence integral over a physical control volume $X(V_i)$ by

$$\int\limits_{\boldsymbol{X}(V_i)} \boldsymbol{\nabla}_{\boldsymbol{x}} \cdot \boldsymbol{F} d\boldsymbol{x} = \int\limits_{V_i} \boldsymbol{\nabla}_{\boldsymbol{\xi}} \cdot (\boldsymbol{N}^T \boldsymbol{F}) d\boldsymbol{\xi} = \sum_{\pm=+,-} \sum_{d=1}^{3} \pm \int\limits_{A_d^{\pm}} (\boldsymbol{N}^T \boldsymbol{F})_d dA_{\boldsymbol{\xi}}, \tag{12}$$

where the $A_d^{\pm}$ are upper and lower faces of cell V_i in the d-th direction. As described in [4], the integrals on the cell faces $A_d^{\pm}$ can be approximated using the following formula for the average of a product in terms of fourth-order accurate face averages of each factor:

$$\langle fg \rangle_{\boldsymbol{i}+\frac{1}{2}\boldsymbol{e}^d} = \langle f \rangle_{\boldsymbol{i}+\frac{1}{2}\boldsymbol{e}^d} \langle g \rangle_{\boldsymbol{i}+\frac{1}{2}\boldsymbol{e}^d} + \frac{h^2}{12} \boldsymbol{G}_0^{\perp,d} \left(\langle f \rangle_{\boldsymbol{i}+\frac{1}{2}\boldsymbol{e}^d} \right) \cdot \boldsymbol{G}_0^{\perp,d} \left(\langle g \rangle_{\boldsymbol{i}+\frac{1}{2}\boldsymbol{e}^d} \right) + O(h^4). \tag{13}$$

Here, $G_0^{\pm,d}$ is the second-order accurate central difference approximation to the component of the gradient operator orthogonal to the d-th direction: $G_0^{\pm,d} \approx \nabla\xi - e^d \frac{\partial}{\partial \xi d}$, and the operator $<\cdot> i + \frac{1}{2}e^d$ $<\cdot> i + \frac{1}{2}e^d$ denotes a fourth-order accurate average over the face centered at $i + \frac{1}{2}e^d$:

$$\langle q \rangle_{\boldsymbol{i}+\frac{1}{2}\boldsymbol{e}^d} = \frac{1}{h^2} \int\limits_{A_d} q(\boldsymbol{\xi}) dA_{\boldsymbol{\xi}} + O(h^4).$$

Alternative expressions to (13) are obtained by replacing the averages $< \int > i + \frac{1}{2}e^d$ and/or $< g > i + \frac{1}{2}e^d$ used in the transverse gradients $G_0^{\perp,d}$ by the corresponding face-centered point-wise values $< \int > i + \frac{1}{2}e^d$ and/or $g\, i + \frac{1}{2}e^d$, respectively.

We therefore have

$$\int_{\boldsymbol{X}(V_i)} \boldsymbol{\nabla}_{\boldsymbol{x}} \cdot \boldsymbol{F} d\boldsymbol{x} = h^2 \sum_{d=1}^{3} \sum_{\pm=+,-} \pm F^d_{\boldsymbol{i}\pm\frac{1}{2}\boldsymbol{e}^d} + O(h^4), \tag{14}$$

where

$$F^d_{\boldsymbol{i}\pm\frac{1}{2}\boldsymbol{e}^d} \equiv \sum_{s=1}^{3} \langle N^s_d \rangle_{\boldsymbol{i}+\frac{1}{2}\boldsymbol{e}^d} \langle F^s \rangle_{\boldsymbol{i}+\frac{1}{2}\boldsymbol{e}^d} + \frac{h^2}{12} \sum_{s=1}^{3} \left(\boldsymbol{G}_0^{\perp,d} \langle N^s_d \rangle_{\boldsymbol{i}+\frac{1}{2}\boldsymbol{e}^d} \right) \cdot \left(\boldsymbol{G}_0^{\perp,d} (\langle F^s \rangle_{\boldsymbol{i}+\frac{1}{2}\boldsymbol{e}^d}) \right), \tag{15}$$

F^s is the s-th component of $\boldsymbol{F}$ and N^s_d is the (s, d)-th element of the matrix $\boldsymbol{N}$. In [4], it is demonstrated that the computation of the face averages $\langle N \frac{s}{d} \rangle i + \frac{1}{2}e^d$ can be reduced to integrals over cell edges. Moreover, assuming that the edge integrals are performed with the same quadratures wherever they appear,

$$\sum_{d=1}^{3} \sum_{\pm=+,-} \pm \int_{A^{\pm}_d} N^s_d dA_{\boldsymbol{\xi}} = 0, \tag{16}$$

which guarantees the freestream property that the divergence of a constant vector field computed by (12) is identically zero.

4. Newton-Krylov solution of the gyrokinetic poisson equation with adiabatic electrons

Although the model (1)-(6) can describe the evolution of electrons just as well as ions, it is often of interest to use a simpler electron model. This is especially the case when performing an explicit time integration, whose time step size would otherwise suffer from the stability restriction resulting from the small electron mass. One such model is the Boltzmann relation

$$n_e = \frac{\langle \sum_i Z_i \bar{n}_i \rangle_j}{\langle \exp(\Phi/T_e) \rangle_j} \exp(\Phi/T_e), \tag{17}$$

where $<\mu> \equiv \sum_k w_{j,k^u}\ r_j, \theta_k)$ denotes the average of μ over the j-th flux surface. Boltzmann relations such as (17) are obtained by integrating the component of the momentum equation in the magnetic field direction of a fluid model neglecting inertial terms; the resulting constant of integration appears as a prefactor that can be chosen to impose an addition constraint. In (17), the prefactor is chosen to maintain charge neutrality on (closed) flux surfaces, which is justified by the fast motion of electrons along field lines.

Because the use of (17) in (8) results in a nonlinear equation, we use a Newton iteration to solve for Φ. In each Newton iteration, a linear solve is performed whose coefficient matrix is the Jacobian $J = J_1 + J_2$, where J_1 is the gyrokinetic Poisson operator and the contribution resulting from (17) is

$$J_2 \equiv \mathrm{diag}_j \left[\frac{\langle \sum_i Z_i \bar{n}_i \rangle_j}{T_e} D_j(\Phi)(I - e^T w_j D_j(\Phi)) \right], \tag{18}$$

where

$$D_j(\Phi) \equiv \frac{\mathrm{diag}_k(\exp(\Phi_{j,k})T_e)}{\langle \exp(\Phi/T_e)\rangle_j}, \tag{19}$$

$$e \equiv (1, 1, ..., 1), \tag{20}$$

$$w \equiv (w_{j,1}, w_{j,2}, ..., w_{j,N}). \tag{21}$$

For domains whose radial width spans many gyroradii, the Jacobian term J_2 dominates J_1. However, J_2 is singular, with a null space comprised of vectors corresponding to functions that are constant on flux surfaces. This implies that the use of a Krylov method to solve the Jacobian system must be modified to avoid the near null space. In the implementation described in the next section, we employ a Bi-Conjugate Gradient Stabilized (BiCGStab) iteration with a two-step preconditioner. The first step projects the current residual onto flux surface averages and applies a tridiagonal solve to obtain a correction that is a function of radius only. The second step of the preconditioner handles the complementary piece of the residual, using a few iterations of a multigrid preconditioned conjugate gradient iteration.

5. Implementation

The algorithms summarized above provide the foundation of a new code named COGENT (COntinuum Gyrokinetic Edge New Technology) for solving the gyrokinetic Vlasov-Poisson system (1)-(6) and (8). The fourth-order, finite-volume, mapped-grid spatial discretization described in Section 3 is combined with a fourth-order Runge Kutta (RK4) time integration. In each function evaluation, the gyrokinetic Poisson equation is solved using the RK4-predicted distribution functions, yielding the electric field needed to compute the phase space velocities (2)-(6).

COGENT is built upon the Chombo library [5] under development by the SciDAC APDEC project to facilitate the creation of structured adaptive mesh refinement (AMR) applications. Although COGENT does not currently utilize Chombo's AMR capabilities, a future development path is nevertheless provided. Chombo provides support for the mapped grid formalism described in Section 3. This includes the construction of discrete metric factors from a user-specified mapping and the computation of fourth-order face-averaged fluxes via (15). COGENT also utilizes Chombo's data containers for mesh-dependent quantities distributed over processors. Such quantities are functions of configuration space (e.g., potential) or phase space (e.g. distribution functions), each of which can be domain decomposed independently. This implies the need for injection and projection operators between configuration/velocity and phase space, which have also been developed in COGENT.

6. Numerical example: Geodesic acoustic modes

As a test of the accuracy of our discretization and code, we consider the calculation of geodesic acoustic modes (GAMs), which are eigenmodes of the gyrokinetic Vlasov-Poisson system [15]. More specifically, a GAM is an ion acoustic wave driven by components of the **E** × **B** force related to the geodesic curvature of field lines on flux surfaces. The radial component of **E** induces a perpendicular flow which, to maintain continuity, results in a density perturbation. The density perturbation generates a current that in turn transports charge across the flux surfaces acting to reverse **E**. The interaction of these processes results in a damped wave. Figure 3 contains plots of ion density (top row) and potential (bottom row) computed by COGENT in the vicinity of an equilibrium flux surface [12] for a sample GAM problem. The times shown are before (left), during (middle) and after (right) one of the direction reversals of the primarily radial electric field. Figure 4 shows the damped oscillation of the potential at a probe located at the point indicated by the "X" in the bottom right panel of Figure 3.

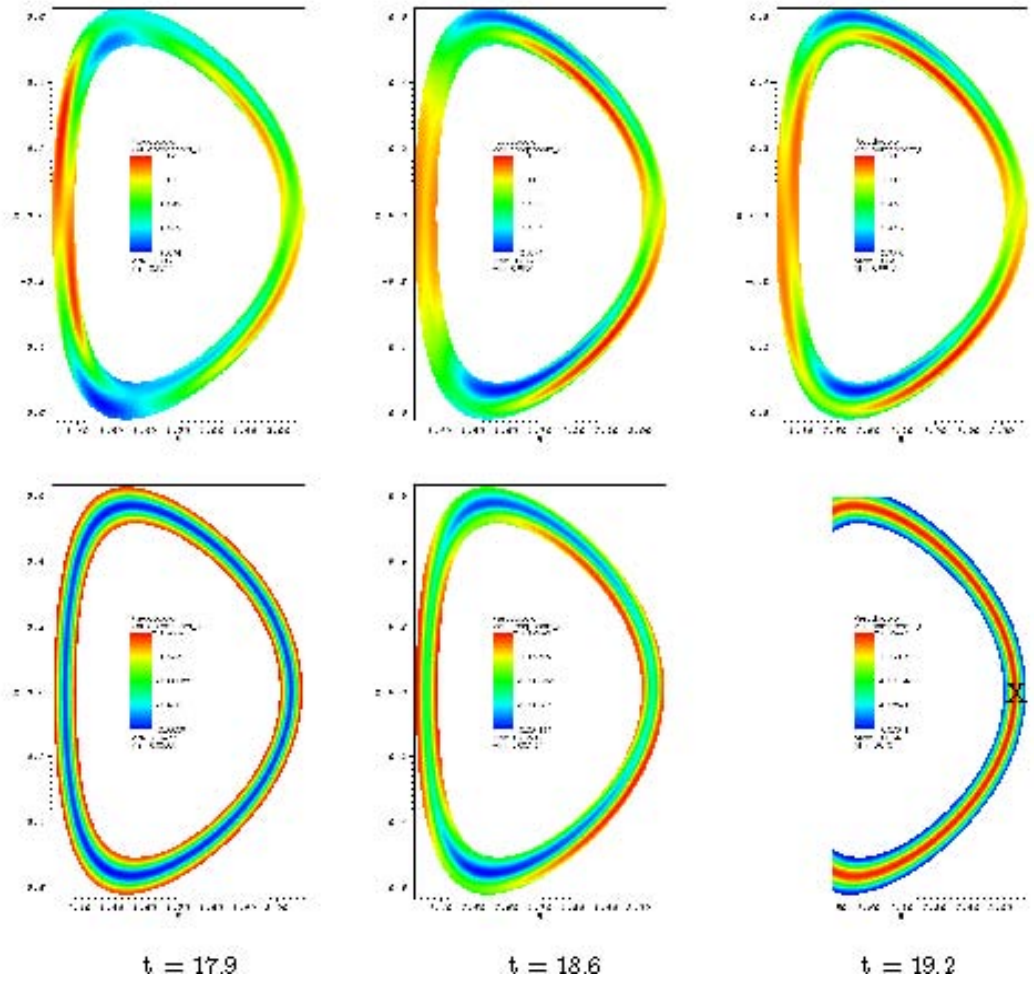

Figure 3. Ion density (top row) and potential (bottom row) in the vicinity of an equilibrium flux surface. The columns correspond to times prior to, during and after a reversal of the electric field.

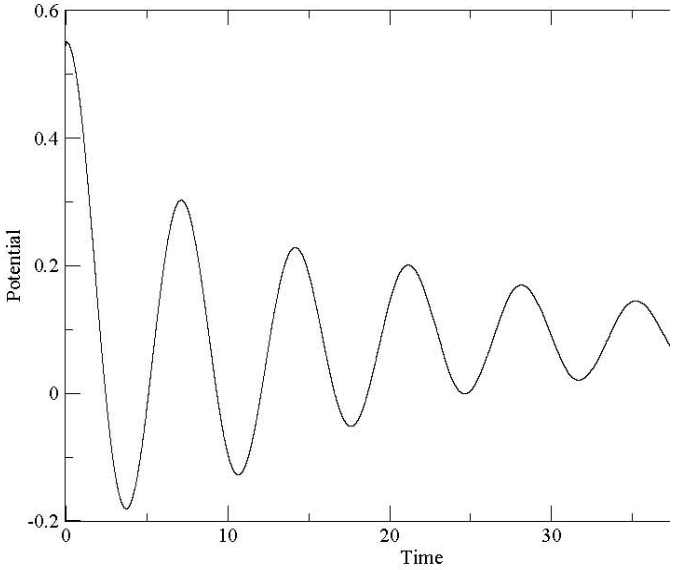

Figure 4. Potential at probe.

In the case of a circular geometry, the GAM frequency and damping rate can be predicted by a dispersion analysis of a linear gyrokinetic equation. In [7], frequencies and damping rates are obtained as functions of the ion thermal velocity v_{ti}, major radius **R**, ratio of electron to ion temperature $\tau = T_e/T_i$, and field line safety factor q. The safety factor q is the number of times a field line winds around the toroidal direction of the torus for each time it winds around the poloidal direction. It thus defines the pitch of a field line, which is related to its geodesic curvature. For large q, the frequency ω and damping rate γ are obtained asymptotically as [7]

$$\omega^2 = \left(\frac{7}{4} + \tau\right) \frac{v_{ti}^2}{R^2} \left[1 + \frac{46 + 32\tau + 8\tau^2}{(7 + 4\tau^2)q^2}\right], \tag{22}$$

$$\gamma = -i\frac{\pi^{1/2}}{2} \frac{v_{ti}}{R} \frac{(R\omega/v_{ti})^6}{(7/4 + \tau)} q^5 \exp\left[-\left(\frac{qR\omega}{v_{ti}}\right)^2\right]. \tag{23}$$

For small q, frequencies and damping rates cannot be expressed in such an analytic form and must instead be obtained by solving for the roots of a nonlinear system of equations. The system includes the resonant responses corresponding to an arbitrary number of toroidal modes.

In Figure 5, the damping rates and frequencies predicted by COGENT are plotted against curves obtained from evaluation of the dispersion model of [7] as reported in

[16] for $\tau = 0$. It is not possible to set the electron temperature to zero in COGENT, so a small value yielding $\tau = 0.1$ is used instead. The theory result includes harmonic resonances through tenth order. Figure 5 also shows the computed rates and frequencies for $\tau = 1$ compared with a curve obtained by evaluating the model of [7]. The latter includes resonances through third order, which is sufficient to converge the result for the range of q values shown.

To investigate the accuracy of the GAM results, we performed a convergence study using a sequence of refined grids and Richardson extrapolation. Beginning with an $8 \times 32 \times 32 \times 8(r \times \theta \times v_{||} \times \mu)$ grid, we generated 3 more grids by refining all phase space dimensions by a factor of two. We then integrated the GK Vlasov-Poisson system to a fixed time on each grid and computed the differences $d_N \equiv ||n_N - n_{N-1}||$, where n_N is the ion density on the N^{th} refinement level, $1 \le N \le 4$, and the norm is the L1, L2 or Max norm. The convergence rates and errors for $N = 3$ and 4 are then estimated by $\rho_N \equiv \log(d_N/d_{N-1})$ and $\epsilon_N \equiv \log(d_N)/(1 + 2^{\rho N})$, respectively. The results are shown in Table 1, where the fourth-order convergence of the error is observed.

In Figure 6, the differences $\epsilon_N \equiv ||n_N - n_4||$ are plotted for $1 \le N \le 3$, approximating the error in the solutions on the first three refined grids by assuming that the solution on the fourth refined grid is exact. The black curve (only whose slope and not vertical position is relevant) indicates fourth-order convergence.

7. Summary

A gyrokinetic code for the predictive simulation the plasma edge of a fusion reactor involves multiple components, including the accurate and efficient advection of full distribution functions in 4D and 5D phase space. We have described here our progress in the development and implementation of a particular discretization of a nonlinear, full-f gyrokinetic Vlasov-Poisson system in mapped coordinates. The approach treats the configuration and velocity components of phase space on an equal footing, using a fourth-order, finite-volume, mapped grid spatial discretization combined with a fourth-order Runge Kutta time integration. The algorithm has been implemented in a new code named COGENT, which is built on the Chombo Adaptive Mesh Refinement library being developed by the SciDAC APDEC project. In COGENT, the phase space, configuration space and velocity space grids may be decomposed independently, allowing degrees of freedom to be deployed most efficiently. The algorithm and code have been tested on geodesic acoustic mode problems in a standard equilibrium magnetic geometry by comparing damping rates and frequencies with those predicted by theoretical dispersion analyses. Convergence tests were also performed to verify the expected increase in accuracy as the phase space grid was refined.

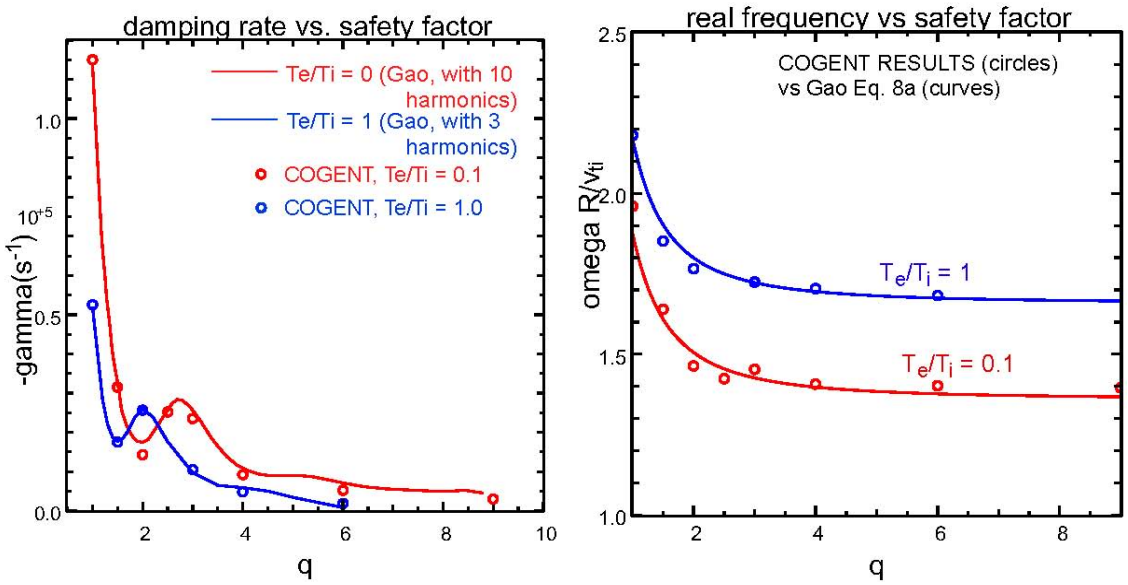

Figure 5. GAM damping rate (left) and frequency (right) as a function of safety factor.

Table 1. Estimated convergence rates and extrapolated errors for a sequence of refined grids

Grid refinement level N	Grid ($r \times \theta \times v_{\|\|} \times \mu$)	Estimated density error conv. rate ρ_N	Richardson extrapolated density error ϵ_N
1	$8 \times 32 \times 32 \times 8$		
2	$16 \times 64 \times 64 \times 16$		
3	$32 \times 128 \times 128 \times 32$	3.8 (L1)	3.37×10^{-7} (L1)
		3.8 (L2)	6.03×10^{-7} (L2)
		4.1 (Max)	1.95×10^{-4} (Max)
4	$64 \times 256 \times 256 \times 64$	4.2 (L1)	1.40×10^{-8} (L1)
		4.1 (L2)	2.95×10^{-7} (L2)
		3.6 (Max)	1.69×10^{-5} (Max)

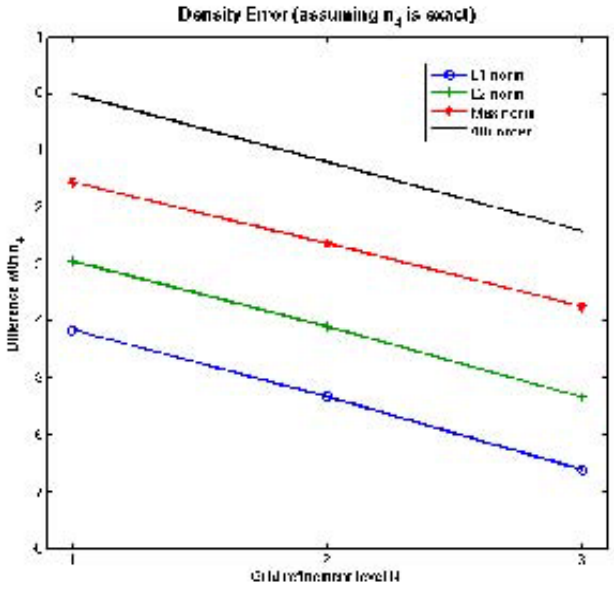

Figure 6. Error as a function of refinement level, assuming the solution on the finest grid is exact. The black curve indicates a fourth-order convergence rate.

References

[1] J. Candy. Gyro. http://fusion.gat.com/comp/parallel/.

[2] J. Candy and R.E. Waltz. Anomalous transport in the DIII-D tokamak matched by supercomputer simulation. *Phys. Rev. Lett.*, 91(4):045001–1–4, 2003.

[3] J. Candy and R.E. Waltz. An Eulerian gyrokinetic-Maxwell solver. *J. Comput. Phys.*, 186:545–581, 2003.

[4] P. Colella, M. R. Dorr, J. A. F. Hittinger, and D. F. Martin. High-order, finite-volume methods in mapped coordinates. *J. Comput. Phys.* Submitted. Also available as Lawrence Livermore National Laboratory report LLNL-JRNL-385708.

[5] P. Colella, D. T. Graves, T. J. Ligocki, D. F. Martin, D. Modiano, D. B. Serafini, and B. Van Straalen. Chombo Software Package for AMR Applications-Design Document. http://seesar.lbl.gov/anag/chombo.

[6] W. Dorland, F. Jenko, M. Kotschenreuther, and B.N. Rogers. Electron temperature gradient turbulence. *Phys. Rev. Lett.*, 85:5579, 2000.

[7] Z. Gao, K. Itoh, H. Sanuki, and J. Q. Dong. Eigenmode analysis of geodesic acoustic modes. *Phys. Plasmas*, 15:072511–1–072511–9, 2008.

[8] T. S. Hahm. Nonlinear gyrokinetic equations for turbulence in core transport barriers. *Phys. Plasmas*, 3(12):4658–4664, 1996.

[9] F. Jenko. Massively parallel Vlasov simulation of electromagnetic drift-wave turbulence. *Comput. Phys. Commun.*, 125:196, 2000.

[10] F. Jenko, T. Dannert, and C. Angioni. Heat and particle transport in a tokamak: Advances in nonlinear gyrokinetics. *Plasma Phys. Contr. F.*, 47:B195, 2005.

[11] M. Kotschenreuther, G. Rewoldt, and W. M. Tang. Comparison of initial value and eigenvalue codes for kinetic toroidal plasma instabilities. *Comput. Phys. Commun.*, 88(128), 1995.

[12] R. L. Miller, M. S. Chu, J. M. Greene, Y. R. Lin-Liu, and R. E. Waltz. Noncircular, finite aspect ratio, local equilibrium model. *Phys. Plasmas*, 5(4):973–978, 1998.

[13] G. D. Porter, R. Isler, J. Boedo, and T. D. Rognlien. Detailed comparison of simulated and measured plasma profiles in the scrape-off layer and edge plasma of diii-d. *Phys. Plasmas*, 7(9):3663–3680, 2000.

[14] Z. Qiu, L. Chen, and F. Zonca. Collisionless damping of short wavelength geodesic acoustic modes. *Plasma Phys. Contr. F.*, 51:012001, 2009.

[15] N. Winsor, J. L. Johnson, and J. M. Dawson. Geodesic acoustic waves in hydro-magnetic systems. *Phys. Fluids*, 11(11):2448–2450, 1968.

[16] X. Q. Xu, E. Belli, K. Bodi, J. Candy, C. S. Chang, R. H. Cohen, P. Colella, A. M. Dimits, M. R. Dorr, Z. Gao, J. A. Hittinger, S. Ko, S. Krasheninnikov, G. R. McKee, W. M. Nevins, T. D. Rognlien, P. B. Snyder, J. Suh, and M. V. Umansky. Dynamics of kinetic geodesic-acoustic modes and the radial electric field in tokamak neoclassical plasmas. *Nucl. Fusion*, 49:065023, 2009.